

# Dataset and Benchmark: Novel Sensors for Autonomous Vehicle Perception

Journal Title  
XX(X):1-11  
©The Author(s) 2024  
Reprints and permission:  
sagepub.co.uk/journalsPermissions.nav  
DOI: 10.1177/ToBeAssigned  
www.sagepub.com/

SAGE

Spencer Carmichael<sup>1</sup>, Austin Buchan<sup>1</sup>, Mani Ramanagopal<sup>1\*</sup>, Radhika Ravi<sup>1\*</sup>, Ram Vasudevan<sup>1,2</sup> and Katherine A. Skinner<sup>1</sup>

## Abstract

Conventional cameras employed in autonomous vehicle (AV) systems support many perception tasks, but are challenged by low-light or high dynamic range scenes, adverse weather, and fast motion. Novel sensors, such as event and thermal cameras, offer capabilities with the potential to address these scenarios, but they remain to be fully exploited. This paper introduces the Novel Sensors for Autonomous Vehicle Perception (NSAVP) dataset to facilitate future research on this topic. The dataset was captured with a platform including stereo event, thermal, monochrome, and RGB cameras as well as a high precision navigation system providing ground truth poses. The data was collected by repeatedly driving two ~8 km routes and includes varied lighting conditions and opposing viewpoint perspectives. We provide benchmarking experiments on the task of place recognition to demonstrate challenges and opportunities for novel sensors to enhance critical AV perception tasks. To our knowledge, the NSAVP dataset is the first to include stereo thermal cameras together with stereo event and monochrome cameras. The dataset and supporting software suite is available at: <https://umautobots.github.io/nsavp>.

## Keywords

Data Sets for SLAM, Localization, Mapping, Sensor Fusion, Computer Vision for Transportation

## 1 Introduction

Frame-based visible spectrum cameras are widely utilized with autonomous vehicles (AVs) due to their relatively low cost, high spatial resolution, and proven suitability for a variety of perception tasks. However, these sensors are challenged by low-light and adverse weather conditions and suffer from several issues including motion blur, limited frame rates, and low dynamic range Zhang et al. (2023b).

Novel sensors, including event and thermal cameras, present advantages that may aid in overcoming these limitations. Event cameras feature high temporal resolution, negligible motion blur, high dynamic range, low power requirements, and low latency Gallego et al. (2022). Thermal cameras sensitive to the Long Wave Infrared (LWIR) spectrum can operate in the absence of visible light and are robust to changes in illumination and visual obscurants such as dust, smoke and fog Judd et al. (2019). However, these novel sensors also present their own challenges. Event cameras represent a new paradigm that is not directly compatible with existing computer vision algorithms. Affordable (uncooled microbolometer) thermal cameras suffer from rolling shutter distortions, significant motion blur, and fixed pattern noise, the latter of which necessitates non-uniformity corrections (NUCs) that may require image interruptions Torres and Hayat (2003).

In this paper, we present the Novel Sensors for Autonomous Vehicle Perception (NSAVP) dataset, which features conventional RGB and monochrome stereo cameras alongside stereo event and stereo thermal cameras. Sequences were collected along two ~8 km routes. Both routes were driven in the forward and reverse directions to

facilitate opposing viewpoint place recognition evaluation. Additionally, one route was driven at three times of day (afternoon, sunset, and night) to capture both benign and challenging lighting conditions. We present benchmarking experiments to evaluate place recognition under illumination changes. The spanned combinations of modality, viewpoint, and lighting are visualized in Fig. 1. We hope the dataset will enable further research that compares or combines conventional and novel sensors for AV perception.

## 2 Related Work

In recent years, there has been increasing interest and availability in AV datasets with non-traditional sensors, including thermal cameras and event cameras. The majority of AV datasets including thermal cameras address pedestrian and object detection Miron et al. (2015); Hwang et al. (2015); Takumi et al. (2017); Teledyne FLIR (2018); Xu et al. (2019); Tumas et al. (2020); Valverde et al. (2021); Farooq et al. (2023) or semantic segmentation Ha et al. (2017); Vertens et al. (2020); Franchi et al. (2024) without supporting localization and mapping tasks. Early exceptions are the KAIST Day/Night Choi et al. (2018) and Brno Urban

<sup>1</sup>Robotics Department, University of Michigan, Ann Arbor, MI 48109 USA

<sup>2</sup>Department of Mechanical Engineering, University of Michigan, Ann Arbor, MI 48109 USA

\*M. Ramanagopal and R. Ravi contributed to this work while employed at University of Michigan.

### Corresponding author:

Spencer Carmichael, 2505 Hayward St., Ann Arbor, MI 48109  
Email: [specarmi@umich.edu](mailto:specarmi@umich.edu)

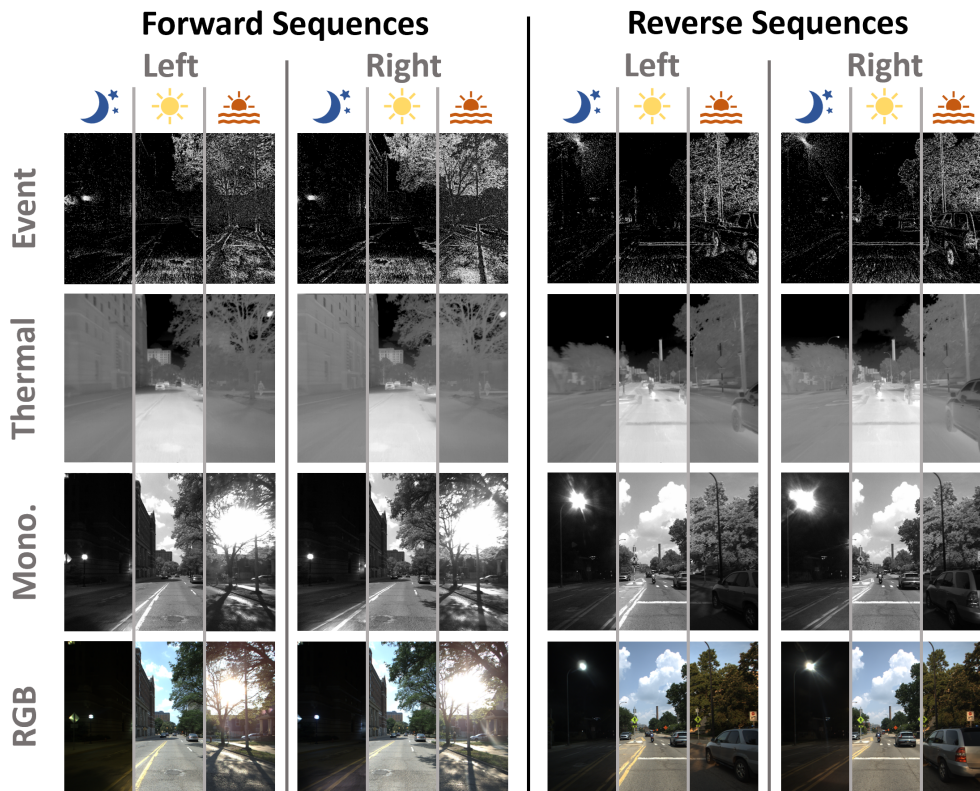


**Figure 1.** Example data from each camera across six sequences capturing two opposing driving directions under three lighting conditions: night, afternoon, and sunset. For each camera, a composite image formed from the three lighting conditions is shown, with event data represented as a time surface Gallego et al. (2022). All the data is from approximately the same location as determined by the provided ground truth poses. These examples highlight the robustness of thermal cameras to illumination changes and of thermal and event cameras to direct sunlight, which produces saturation and blooming in conventional cameras.

Ligocki et al. (2020) datasets, which include data from lidar and RTK GNSS systems serving as depth and pose ground truth, respectively. However, the KAIST Day/Night and Brno Urban datasets only provide monocular thermal cameras and do not include event or monochrome cameras.

Similarly, many earlier AV datasets including event cameras target tasks such as object detection Sironi et al. (2018); De Tournemire et al. (2020); Perot et al. (2020), image reconstruction Scheerlinck et al. (2019); Rebecq et al. (2021), and lane extraction Cheng et al. (2019). The DDD17 dataset Binas et al. (2017) was created primarily to investigate event-based end-to-end driving with vehicle control data, but it also includes GPS position data and overlapping sequences, making it the first dataset suitable for event-based place recognition evaluation. The DDD20 dataset Hu et al. (2020) later expanded upon the DDD17 dataset, and concurrently the Brisbane-Event-VPR dataset Fischer and Milford (2020) was released to allow large-scale event-based place recognition to be tested under varied illumination and weather conditions. The MVSEC dataset Zhu et al. (2018), which features multiple platforms, including a car, is the first dataset to include synchronized stereo event cameras. However, the event cameras have a low 0.09 MP resolution and narrow 10 cm baseline owing to the sensor rig being designed to fit small platforms. As a result, event-based stereo depth estimation is limited in the MVSEC AV sequences Hadviger et al. (2021). In response, the DSEC dataset Gehrig et al. (2021) is explicitly designed for event-based stereo depth estimation with higher resolution (0.31

MP) event cameras and a larger 51 cm baseline. However, while useful for that specific task, the DSEC dataset does not provide ground truth trajectories and is therefore unsuitable for visual odometry or place recognition evaluation. The proposed NSAVP dataset also includes stereo event cameras with a wide baseline and additionally offers overlapping sequences and precise ground truth pose enabling both place recognition and visual odometry evaluation.

In the past two years, several AV datasets have been published with thermal or event cameras and ground truth trajectories. ViViD++ Lee et al. (2022) is the first to have both modalities, with a single camera of each, followed by ECMD Chen et al. (2023), which includes a monocular thermal camera together with stereo event cameras. STheReO Yun et al. (2022), and subsequently MS<sup>2</sup> Shin et al. (2023), are the first to provide asynchronous and synchronous stereo thermal camera data, respectively. NTU4DRadLM Zhang et al. (2023a) is the first to pair a thermal camera with a 4D radar system. Similar to MVSEC, the M3ED Chaney et al. (2023) dataset includes a stereo event camera attached to a single sensor rig placed on multiple platforms of varied sizes. Again, the small baseline (12 cm) limits stereo depth estimation in typical AV environments, although this is mitigated by the cameras' high 0.92 MP resolution Chaney et al. (2023). Similar to DDD17 and DDD20, MA-VIED Mollica et al. (2023) provides vehicle control data alongside a monocular event camera, but includes a higher resolution event camera, higher quality pose ground truth, and the addition of a monochrome

**Table 1.** Comparison with AV datasets which include event or thermal cameras and support localization and mapping tasks. For multi-platform datasets, the table reflects the AV sequences only. The proposed NSAVP dataset is the only to include each camera modality and to include stereo thermal cameras together with stereo event and monochrome cameras.

Dataset	Cameras (Megapixels $\times$ Quantity)				Ground Truth Pose/Position
	Thermal	Event	Monochrome	RGB	
DDD17 <a href="#">Binas et al. (2017)</a>		$0.09 \times 1$	$0.09 \times 1^*$		★
MVSEC <a href="#">Zhu et al. (2018)</a>		$0.09 \times 2$	$0.09 \times 2^*$ $0.36 \times 2$		★
KAIST Day/Night <a href="#">Choi et al. (2018)</a>	$0.31 \times 1$			$1.23 \times 2$	★★★
Brno Urban <a href="#">Ligocki et al. (2020)</a>	$0.33 \times 1$			$2.30 \times 4$	★★
DDD20 <a href="#">Hu et al. (2020)</a>		$0.09 \times 1$	$0.09 \times 1^*$		★
Brisbane-Event-VPR <a href="#">Fischer and Milford (2020)</a>		$0.09 \times 1$		$0.09 \times 1^*$ $2.07 \times 1$	★
DSEC <a href="#">Gehrig et al. (2021)</a>		$0.31 \times 2$		$1.56 \times 2$	
ViViD++ <a href="#">Lee et al. (2022)</a>	$0.33 \times 1$	$0.31 \times 1$		$1.31 \times 1$	★★
STheReO <a href="#">Yun et al. (2022)</a>	$0.33 \times 2$			$0.72 \times 2$	★★★
M3ED <a href="#">Chaney et al. (2023)</a>		$0.92 \times 2$	$1.02 \times 2$	$1.02 \times 1$	★★
MS <sup>2</sup> <a href="#">Shin et al. (2023)</a>	$0.33 \times 2$			$5.01 \times 2$	★
Stereo Visual Localization <a href="#">Hadviger et al. (2023)</a>		$0.31 \times 2$		$3.15 \times 2$	★★★
MA-VIED <a href="#">Mollica et al. (2023)</a>		$0.31 \times 1$	$2.30 \times 1$		★★★
NTU4DRadLM <a href="#">Zhang et al. (2023a)</a>	$0.33 \times 1$			$0.31 \times 1$	★★
ECMD <a href="#">Chen et al. (2023)</a>	$0.33 \times 1$	$0.09 \times 2$ $0.31 \times 2$		$0.09 \times 2^*$ $2.30 \times 2$	★★★
<b>NSAVP</b>	$0.33 \times 2$	$0.31 \times 2$	$1.56 \times 2$	$1.25 \times 2$	★★★

★: Non-differential GNSS or SLAM-derived, ★★: RTK or PPK GNSS Position, ★★★: RTK or PPK GNSS/IMU 6-DoF Pose  
\*: Frame captured by DAVIS event camera

camera, IMU, and wheel odometer. Finally, the Stereo Visual Localization dataset [Hadviger et al. \(2023\)](#) addresses the gap left by DSEC by capturing AV sequences with a wide baseline stereo event camera and ground truth poses from a dual antenna RTK GNSS/IMU system. While these datasets encompass a variety of sensor suites, none include stereo thermal cameras together with stereo event or monochrome cameras.

Table 1 gives a comparison with all AV datasets that include event or thermal cameras and support localization and mapping tasks. Our contributed dataset is the first to include stereo thermal cameras together with stereo event and monochrome cameras, and it provides precise time synchronization between all sensors and highly accurate ground truth poses. Thermal and event cameras complement each other in terms of robustness to motion and low-light conditions making the fusion of these modalities promising. Additionally, monochrome cameras are more sensitive than RGB cameras and do not suffer from debayering artifacts making them a better comparison point to novel sensors in low-light conditions. Moreover, by repeatedly driving large-scale routes in opposing directions, our dataset is uniquely able to support opposing viewpoint place recognition evaluation. Finally, we note that ground truth object bounding boxes and pixelwise semantic labels could be added to our dataset in the future, similar to the extensions of DDD17 [Alonso and Murillo \(2019\)](#), MVSEC [Hu et al. \(2021\)](#), and DSEC [Sun et al. \(2022\)](#).

### 3 Platform and Sensors

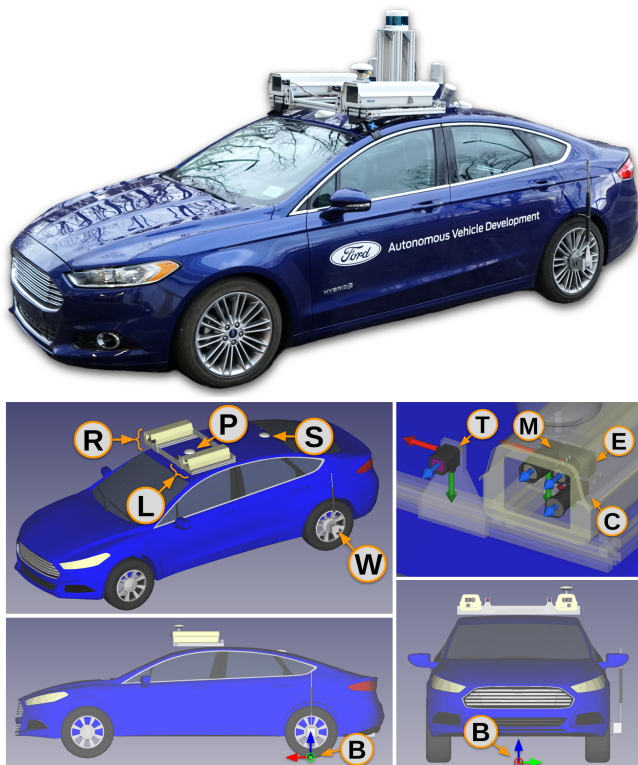
The proposed dataset was collected using a Ford Fusion platform with a custom sensor suite as pictured in Fig. 2. The sensor suite includes stereo pairs of each camera detailed in Table 2, a Protomips Thunderbolt GM200 grandmaster clock, and an Applanix POS-LV 420 navigation system featuring a dual antenna GNSS receiver, IMU, and wheel encoder. We use the GM200 for time synchronization, as described in section 4.2, and the POS-LV 420 to obtain 200 Hz ground truth poses of the vehicle’s ‘base link’ frame, as described in section 4.4. An on-board compute and network system performs sensor initialization, configuration, and data logging. The compute system with a Ryzen 9 5950X 3.4GHz 16-Core CPU, 64GB DDR4 RAM, 4TB NVMe solid-state drive, and 10Gbit Ethernet ports was sufficient to handle saving the 3Gbps+ raw data stream to disk.

Figure 2 shows the locations of the sensors on the vehicle and the relevant coordinate frames. The visible spectrum cameras are housed in enclosures on either side of the car in a mirrored configuration and are clustered tightly together within each enclosure to minimize parallax. The thermal cameras sit outside of the enclosures, as the enclosure glass is opaque in the LWIR spectrum. In selecting stereo baselines we considered triangulation error and field of view (FOV) overlap. We selected relatively large baselines to reduce triangulation error, placed the thermal cameras on the inside due to their narrower field of view, and placed the event cameras on the outside due to their lower resolution. Figure 3

**Table 2.** Specifications of the stereo cameras included in the sensor suite.

Type	Camera Model	Lens Model	Stereo Baseline (meters)	FOV (H × V)	Resolution (W × H)	Rate (Hz)	Frame Readout
Monochrome (CMOS)	FLIR BFS-PGE-16S2M (FLIR Blackfly S GigE)	Computar A4Z2812CS-MPIR	0.90	70° × 55°	1440 × 1080	20.14	Global
RGB (CMOS)	FLIR BFS-PGE-50S5C (FLIR Blackfly S GigE)	Fujinon HF6XA-5M	1.00	70° × 60°	1224 × 1024	20.14	Global
Thermal (Uncooled VOx Microbolometer)	FLIR 40640U050-6PAAX (FLIR ADK)	NA (Integrated)	0.64	50° × 40°	640 × 512	60.42	Rolling
Event (DVS)	Inivation DVXplorer	NA (Included with Camera)	1.00	70° × 50°	640 × 480	NA	NA

NA: Not applicable



**Figure 2.** Vehicle Sensor Platform<sup>1</sup>. The labeled vehicle diagram shows the position and orientation of the symmetric **Left** and **Right** groups of vision sensors, **Primary** and **Secondary** POS-LV 420 antennas, and POS-LV 420 **Wheel** encoder. The sensor detail diagram shows the left sensor group, with a **Thermal** camera, **Event** camera, **Monochrome** camera, and **Color** (RGB) camera. The left and front vehicle views show the location of the system reference **Base** link frame. Coordinate frames use red, green, and blue arrows for x, y, and z axes respectively.

compares depth estimate uncertainty between the thermal and event stereo pairs included in our dataset and the datasets listed in Table 1. Our configuration achieves the lowest predicted depth uncertainty.

## 4 Data Collection

### 4.1 Camera Settings

The monochrome and RGB cameras are set to utilize auto-exposure and auto-gain such that exposure is increased first, up to a maximum of 15 ms, and then gain is increased, up to

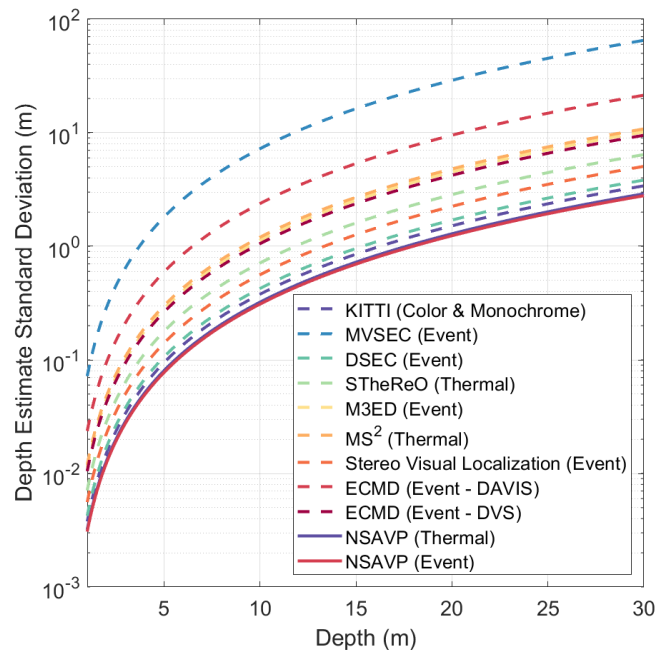


**Figure 3.** Comparison of thermal and event stereo depth estimate uncertainty across AV datasets assuming the error model described in [Matthies and Shafer \(1987\)](#). Conventional stereo cameras from the established KITTI dataset [Geiger et al. \(2013\)](#) are also included for reference. NSAVP achieves the lowest predicted depth uncertainty.

a maximum of 18 dB. We enable auto-white balancing and gamma correction in the RGB cameras and disable gamma correction in the monochrome cameras. To reduce bandwidth and storage requirements, we enable  $2 \times 2$  pixel binning in the RGB cameras, resulting in the resolution given in Table 2. The event cameras' bias sensitivity is set to the default preset.

The thermal cameras are set to perform NUCs automatically<sup>2</sup>. Each NUC produces a  $\sim 0.5$  second period of dropped frames. NUCs occur every  $\sim 3$ -5 minutes throughout the dataset and are most frequent in the afternoon sequences. Notably, there are no instances in the dataset in which a NUC occurs simultaneously in the left and right thermal cameras. This uninterrupted availability of thermal images could allow, for example, a stereo thermal odometry method to temporarily propagate scale with one camera during a NUC on the other.

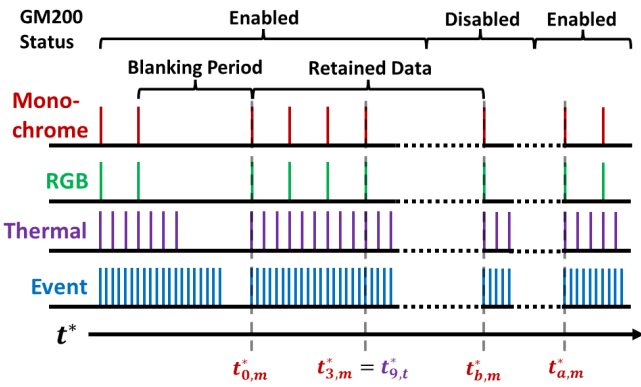


**Figure 4.** Visualization of time synchronization signals sent to each camera modality. For simplicity, single vertical lines are used to represent the square wave edges (rising or falling) each sensor responds to. The durations of the blanking period and frequency of the event camera signal are not to scale.

## 4.2 Camera Time Synchronization

To achieve synchronized image capture and timestamps we trigger the cameras with an Arty Z7 FPGA development board connected to the cameras through a custom adapter PCB. The RGB and monochrome cameras receive a nominal 20 Hz square wave and the thermal cameras receive a nominal 60 Hz square wave such that every RGB and monochrome image, and every third thermal image, are captured simultaneously. Specifically, the signals trigger the start of exposure in the RGB and monochrome cameras and the start of readout in the thermal cameras. The event cameras receive a 10 kHz square wave, which advances their timestamps on each falling edge. These signals are visualized in Fig. 4.

To synchronize the timestamps across all modalities we employ a careful strategy. The GM200 is able to synchronize the monochrome and RGB camera clocks with International Atomic Time (TAI) via the Precision Time Protocol (PTP) with nanosecond accuracy, but it can operate only while stationary. We ensure the vehicle is parked at the beginning and end of each recorded sequence to allow the use of the GM200, and we disable the GM200 while in motion. We poll and record the PTP status of the cameras during data collection. The thermal and event cameras do not support PTP, so we apply a blanking period to each trigger signal while the GM200 is enabled to provide an association across all cameras. The blanking period duration varies to satisfy different interface requirements, but the end of the blanking period is aligned across all cameras and can be programmatically identified after collection in the recorded data. The blanking period appears as missing frames in the RGB, monochrome, and thermal cameras, and resets the event camera clock to start from zero at the end of the blanking period.

With this strategy we are able to correct all timestamps in post-processing. We define the aligned edge at the end of the blanking period as trigger 0. For each frame-based camera, we assign trigger indices to images by counting forward from trigger 0 while accounting for dropped frames. Let  $t_{0,m}$  and  $t_{0,m}^*$  denote the camera clock and TAI timestamps of the left monochrome image at trigger 0, respectively. The blanking period is applied while the GM200 is enabled and therefore

$t_{0,m} \approx t_{0,m}^*$ . Similarly, let  $t_{a,m} \approx t_{a,m}^*$  denote the timestamp of a left monochrome image, with trigger index  $a$ , captured after the GM200 is re-enabled at the end of the sequence. The TAI timestamp of an image shortly before the GM200 is re-enabled can be estimated as  $\tilde{t}_{b,m}^* = t_{a,m}^* - T(a - b)$ , where  $T$  is the effective trigger signal period derived from the camera clock timestamps. To correct for clock drift during the period where the GM200 is disabled, the TAI timestamps for all left monochrome images between trigger 0 and  $b$  are estimated as follows:

$$\tilde{t}_{i,m}^* = t_{0,m}^* + (t_{i,m} - t_{0,m}^*)c_m, \quad c_m = \frac{\tilde{t}_{b,m}^* - t_{0,m}^*}{t_{b,m} - t_{0,m}^*} \quad (1)$$

All images before trigger 0 and after trigger  $b$  are dropped. To validate the above procedure, we repeat it with each RGB and monochrome camera and compare the resulting TAI timestamps at each trigger index. Across the dataset, the average disagreement is on the order of 10  $\mu$ s and the maximum is 0.22 ms.

After the left monochrome timestamps are corrected, they are directly applied to all simultaneously triggered images and used to interpolate all nonsimultaneous image timestamps. That is,  $\tilde{t}_{3i,t}^* = \tilde{t}_{i,m}^*$  where  $\tilde{t}_{3i,t}^*$  denotes the TAI timestamp assigned to the left thermal image at trigger index  $3i$ , etc.

Given that the event camera clocks are reset at the end of the blanking period and are in lockstep with the FPGA's clock, the TAI timestamp of the  $i$ th event  $t_{i,e}^*$  can be estimated from its camera clock timestamp  $t_{i,e}$  as:

$$\tilde{t}_{i,e}^* = t_{0,m}^* + t_{i,e}c_e, \quad c_e = \frac{t_{a,m}^* - t_{0,m}^*}{a\tilde{T}} \quad (2)$$

where  $\tilde{T}$  is the nominal period of the monochrome camera trigger signal, as configured on the FPGA.

## 4.3 Camera Calibration

We use Kalibr [Furgale et al. \(2013\)](#) to perform simultaneous calibration of the intrinsic and extrinsic parameters across all eight cameras, applying the pinhole camera model and radial-tangential distortion model to each camera. To facilitate this multi-spectral calibration, we create a unique calibration board. Following existing work on passive thermal calibration boards [EISheikh et al. \(2023\)](#), our board is constructed with two materials of different emissivities and we heat it to increase the contrast between them. Specifically, the board is composed of an aluminum sheet with black vinyl adhered to it and cut to the shape of a grid of AprilTags [Olson \(2011\)](#). The high emissivity vinyl and low emissivity aluminum primarily emit and reflect IR radiation, respectively. We apply a heat gun to the board prior to recording a calibration sequence. When heated, the vinyl appears bright in the thermal images while the aluminum reflects the generally colder surroundings and appears darker. While recording the calibration sequence, we move the board slowly to mitigate the impact of the thermal cameras' motion blur and rolling shutter effect.

The AprilTag detection employed by Kalibr can operate directly on monochrome images and RGB images converted to grayscale. To prepare the thermal images for AprilTag detection we truncate, invert, and normalize them to an 8-bit

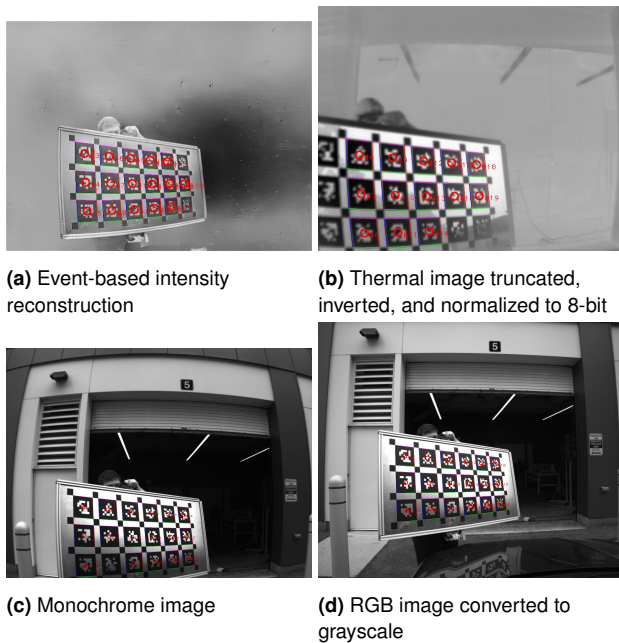


**Figure 5.** Calibration board AprilTag detections (denoted with red circles) in synchronized images captured or reconstructed across all modalities on the left side of the vehicle.

range. We use e2calib [Muglikar et al. \(2021\)](#) to reconstruct intensity images from events that are synchronized with the other modalities. Figure 5 shows simultaneous AprilTag detections across all modalities. As noted with similar calibration boards [Ursine et al. \(2012\)](#); [St-Laurent et al. \(2017\)](#), reflections off the aluminum surface can interfere with detection. However, by using an AprilGrid rather than a checkerboard pattern [Huai et al. \(2023\)](#), we are able to make use of partial detections of the board despite reflections and occlusions, as shown in Fig. 5b. We ultimately obtain zero mean reprojection errors with standard deviations less than or equal to 0.6 pixels, except along the dominant direction of motion in the thermal camera, where the standard deviation is 1 pixel.

#### 4.4 Ground Truth

We log data from the POS-LV 420 system at 200 Hz over the course of entire data collection sessions that span multiple recorded sequences. To aid IMU alignment in both forward and backward processing of the data, we begin each session by remaining static for 5 minutes and then performing dynamic movements (figure-eights and linear accelerations) and end each session with the same stages in the opposite order. We post-process the logged data with the Applanix POSpac Mobile Mapping Suite V8.8<sup>3</sup> using the IN-Fusion Smartbase mode [Hutton et al. \(2008\)](#), which employs a tightly-coupled Kalman filter to fuse data from all components of the system, along with atmospheric errors interpolated from multiple nearby base stations, to produce a highly accurate pose trajectory estimate of the vehicle base link frame relative to the earth-centered earth-fixed (ECEF) frame. The estimated standard deviations are on average 2 cm in east and north, 5 cm in height, 0.005° in roll and pitch, and 0.03° in yaw. To relate the POS-LV 420 output with the cameras we manually measure the relative pose between the

**Table 3.** Sequences collected. The sequence names follow the pattern <route>.<direction><lighting><index>.

Sequence Name	Route	Direction	Lighting	Path Length (km)	Duration (minutes)	Total Size (GB)
R0_FA0	R0	Forward	Afternoon	8.3	17.5	139
R0_FS0			Sunset		15.2	104
R0_FN0			Night		14.8	92
R0_RA0	R0	Reverse	Afternoon	8.3	21.5	162
R0_RS0			Sunset		17.1	127
R0_RN0			Night		15.5	92
R1_FA0	R1	Forward	Afternoon	8.6	27.5	217
R1_DA0		Forward, Diverge			20.8	173
R1_RA0		Reverse			22.4	169
C1		Calibration			2.2	16

vehicle base link frame and each camera frame. By using laser levels to aid in measurement, we expect the accuracy of the manually measured extrinsics to be within  $\pm 5$  mm and  $\pm 3^\circ$ . The POS-LV 420 timestamps are output in GPS time, have nanosecond accuracy, and are easily converted to TAI.

#### 4.5 Routes and Sequences

Data was collected along two  $\sim 8$  km routes R0 and R1 as shown in Fig. 6. The routes pass through suburban areas, characterized primarily by trees and residential buildings, and urban areas, which include large multi-story buildings. Each route was driven in both the forward and reverse directions to support opposing viewpoint place recognition evaluation. The routes cover four and two lanes roads and were mainly driven in the left lane with only the lane line dividing opposing directions. However, some portions include an additional lateral shift due to medians, turn lanes, and occasional lane shifts, which provides a further challenge for place recognition. Figure 6 shows the routes, denotes their various stages, and defines the forward and reverse directions.

Route R1 was driven in the afternoon while R0 was driven under three lighting conditions: afternoon, sunset, and night. The afternoon sequences are bright and have high thermal contrast, while the sunset and night sequences feature high dynamic range, low thermal contrast, and low light scenes. Figure 1 shows data from each sequence recorded along route R0. Route R1 was driven in the forward direction twice, with one sequence including divergences from the route to allow place recognition to be evaluated with true negatives (i.e., places in the query sequence with no match in the reference sequence). Table 3 summarizes all sequences collected.

#### 4.6 Known Issues

We have identified a few issues that may impact processing. We expect the overall impact to be negligible, but we mention them here for completeness. First, the auto-algorithms used by the RGB and monochrome cameras to control exposure, gain, and white balancing, run independently in each camera leading to potential differences between the left and right images of each stereo pair. However, differences in gain

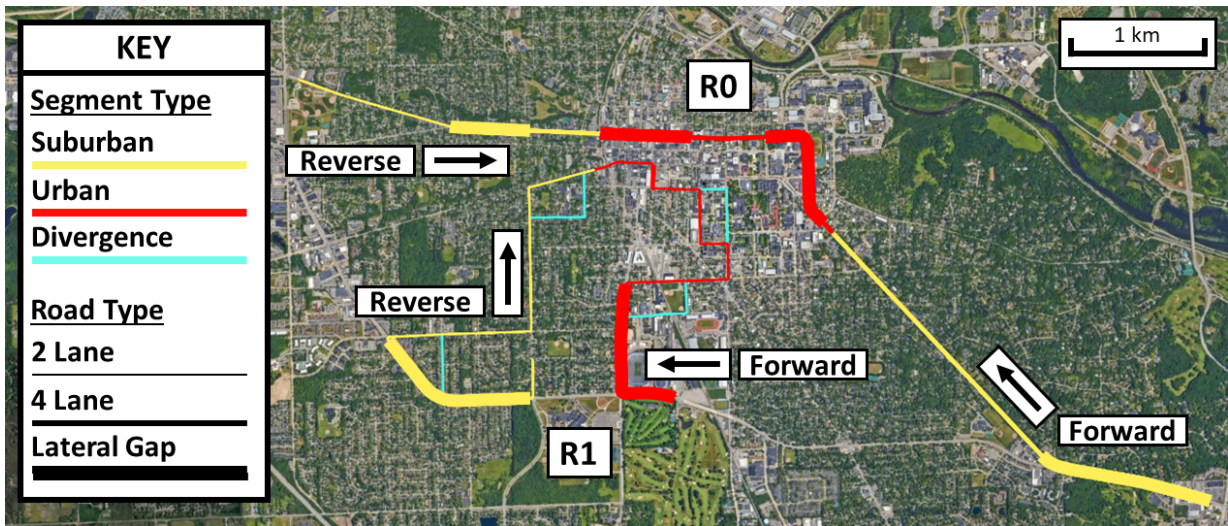


**Figure 6.** Data collection routes R0 and R1. Scene types and divergences are distinguished with different colors. Road widths and lateral gaps between opposing lanes are distinguished with different line thicknesses. The forward and reverse labels denote the directions used in the sequence names.

and exposure can be approximately corrected using the values recorded for these quantities per image as described in section 5. Second, outside of the NUCs, 1-2 frames are dropped from the thermal cameras  $\sim 10$ -20 times per sequence. Finally, a few insects collided with the visible camera enclosures in the route R0 sequences collected at night. These insects appear as small out-of-focus smudges at the top of each visible camera’s FOV.

## 5 Data Organization and Format

The dataset is available for download at the University of Michigan Library’s Deep Blue Data repository<sup>4</sup>. The data is organized by sequence. Within each sequence, the data from each sensor is provided as a separate HDF5<sup>5</sup> file (abbreviated H5) and the camera calibration results (section 4.3) and manually measured extrinsics (section 4.4) are given as human-readable YAML<sup>6</sup> files. We use the H5 file format as it is guaranteed to be backward compatible, allows heterogeneous data to be stored in a single file, and supports lossless compression and efficient partial data access. The content of these files is summarized below; a more detailed description is available in our software tools repository (section 6).

The camera data filenames follow the pattern `<sequence name>_<sensor>_<side>.h5` where `<side>` is left or right and `<sensor>` denotes the camera type or model as `mono` (monochrome), `rgb` (RGB), `adk` (thermal), or `dvxplorer` (event). Each of the frame-based camera files include a H5 group, `image_raw`, containing raw images and their corresponding timestamps as H5 datasets `images` and `timestamps`. Similarly, the event camera files include a H5 group, `events`, which contains a separate H5 dataset for each event field: `x_coordinates`, `y_coordinates`, `timestamps`, and `polarities`. Fixed quantities relating to the images and events, such as width, height, and encoding, are attached as H5 attributes to the `image_raw` and `events` H5 groups. Additionally, the frame-based camera files include an `image_meta` H5 group containing per-image metadata

such as exposure, gain, or NUC status. Comprehensive camera settings are also attached as attributes to the root H5 group in the monochrome, RGB, and event camera files.

The ground truth poses are provided in a file named `<sequence name>_applanix.h5`. This file includes a `pose_base_link` H5 group containing H5 datasets positions, quaternions, and timestamps, which give the poses of the base link frame in the ECEF frame.

## 6 Software Tools

To facilitate efficient use of the dataset we provide a set of software tools<sup>7</sup>. To ensure cross-platform compatibility, we include Dockerfiles alongside instructions to build Docker images capable of running all provided code.

The `conversion` ROS package includes scripts to combine H5 files and convert a combined H5 file to a rosbag or to directories containing human readable CSV files and PNG images. Reading the data from the rosbag format, the `preprocessing_and_visualization` ROS package includes scripts that demonstrate common pre-processing operations (debayering, like and cross modality rectification, cropping, etc.) and visualize the camera data and ground truth pose as shown in Fig. 7.

Additionally, we include example scripts applying and evaluating a place recognition algorithm with the dataset, utilizing the H5 format directly. The example uses NetVLAD [Arandjelovic et al. \(2016\)](#) and produces the same results given for this algorithm in section 7. As part of this example, we also provide an algorithm-agnostic GUI that can be used to visualize place recognition results and step through individual matches. Figure 8 shows the GUI displaying the results of running NetVLAD with the left thermal images from the R0\_RA0 sequence and R0\_RN0 sequence as described in the following section.

## 7 Place Recognition Benchmark

To highlight some of the research challenges our dataset poses, we demonstrate a use case of our dataset on the task

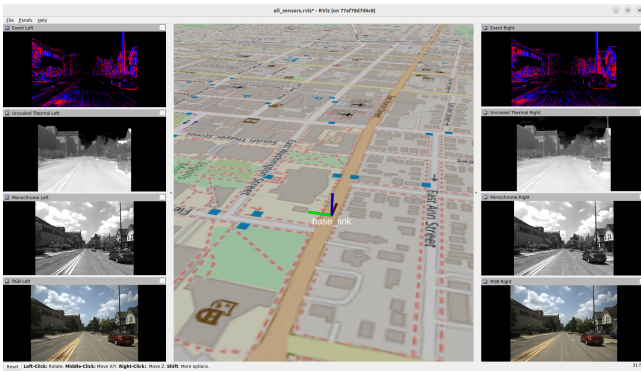


**Figure 7.** RViz visualization of ground truth pose and pre-processed camera data (map sourced from OpenStreetMap<sup>8</sup>).

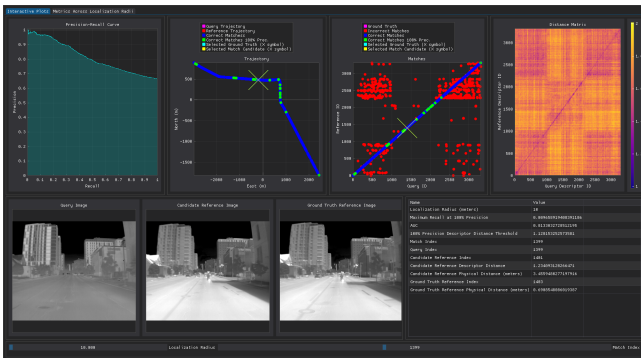


**Figure 8.** Place recognition evaluation GUI including the following components from left-to-right and top-to-bottom: precision-recall curve, plot of correct matches along the trajectory, plot of candidate and ground truth matches, distance matrix, query image, candidate reference image, ground truth reference image, table of place recognition metrics, localization radius slider, and match index slider.

of place recognition. Place recognition is the problem of determining whether a given place, represented with a query, matches a specific place within a database of references. We evaluate the opposing viewpoint focused method LoST-X Garg et al. (2018) and the seminal method NetVLAD Arandjelovic et al. (2016). As in Garg et al. (2018), we select input images to be 2 meters apart according to the ground truth position data, and additionally augment LoST-X and NetVLAD with sequence matching Milford and Wyeth (2012) using a sequence length of 51 (denoted with +SM). We apply both approaches to the left RGB images of each selected sequence and also run NetVLAD with the left thermal images (denoted with +T). The thermal images are truncated and converted to 8-bit at the input to NetVLAD.

In all tests, the reference database is formed using a 6.7 km subset of the R0\_RA0 sequence. The queries are taken from the R0\_RS0, R0\_RN0, R0\_FA0, and R0\_FN0 sequences using the same subset. For succinctness, the sequence pairs will be referred to by the sequence the queries are drawn from. We use a 10 meter localization radius (denoted with  $r = 10$  m) to determine correct matches for the sequences driven in the same direction as the reference database and, following Garg et al. (2018), we use an 80 meter localization radius (denoted with  $r = 80$  m) for the opposing viewpoint sequences.

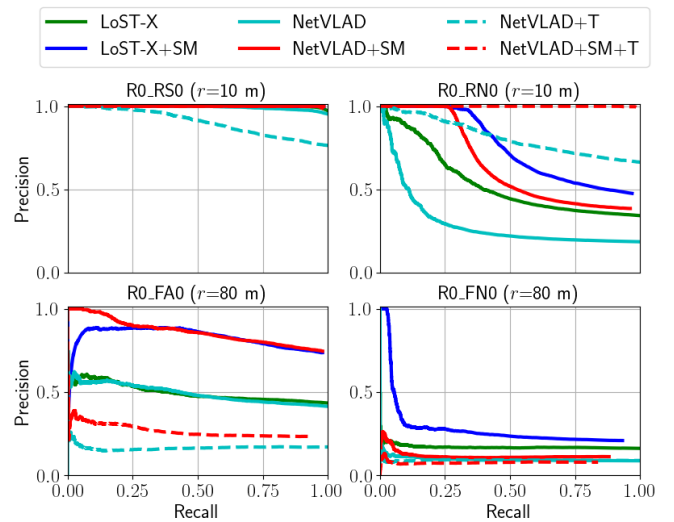


**Figure 9.** Precision-recall curves of each method on the selected sequence pairs.

Figure 9 shows precision-recall curves of each tested method on the selected sequence pairs. All methods perform well with the R0\_RS0 sequence, which was driven in the same direction and under similar lighting conditions as the reference database. The R0\_RN0 sequence is more difficult, due to the drastic lighting change and poor visibility in the RGB camera. This demonstrates a common failure case for visible spectrum cameras (RGB and monochrome) deployed for AV perception. This issue can be overcome by using thermal images instead, as shown by the NetVLAD+SM+T result. Still, the opposing viewpoint sequences, R0\_FA0 and R0\_FN0, provide a further challenge and the limited results on these sequences indicate there is significant room for further development with both visible spectrum and thermal cameras. The NSAVP dataset provides a resource for the research community to investigate this open challenge.

## 8 Summary and Future Work

We introduce the NSAVP dataset, which features stereo event, thermal, monochrome, and RGB cameras and captures opposing viewpoints and varied lighting conditions. We believe the dataset presents unique opportunities to apply novel sensors to AV perception. We demonstrate an example use case of this dataset towards the task of place recognition. In the near future, we aim to expand the sensor suite to include lidar and IMU sensors and additionally collect data in adverse weather conditions including snow and rain, which further challenge conventional sensors.

### Acknowledgements

The authors wish to thank Martin Ward for his work in prototyping the hardware design, and Rahul Agrawal, Vivek Jaiswal, Dhiraj Maji, and Xun Tu for their contributions to the data collection process and software.

### Declaration of conflicting interests

The Authors declare that there is no conflict of interest

## Funding

The authors disclosed receipt of the following financial support for the research, authorship, and/or publication of this article: This work was supported by the Ford Motor Company via the Ford-UM Alliance under award N028603.

## Notes

1. CAD sources:  
Monochrome and RGB camera models  
<https://www.flir.com/support-center/iis/machine-vision/knowledge-base/technical-documentation-bfs-gige/>  
Thermal camera model  
<https://www.flir.com/support/products/adk/?pn=ADK&vn=40640U050-6PAAX#Downloads>  
Event camera model  
<https://grabcad.com/library/davis346-event-camera-1>  
Ford Fusion model (released with the Ford Multi-AV Seasonal Dataset Agarwal et al. (2020))  
[https://github.com/Ford/AVData/blob/master/fusion\\_description/meshes/Ford\\_fusion.obj](https://github.com/Ford/AVData/blob/master/fusion_description/meshes/Ford_fusion.obj)
2. The NUC discussed in this section involves a shutter which closes to present a uniform thermal signal to the sensor array. Such a NUC is referred to as calibration-based. The thermal cameras also continuously perform a scene-based NUC.
3. <https://www.applanix.com/products/pospac-mms.htm>
4. <https://deepblue.lib.umich.edu/data/collections/v118rf157>
5. <https://www.hdfgroup.org/solutions/hdf5/>
6. <https://yaml.org/>
7. [https://github.com/umautobots/nsavp\\_tools](https://github.com/umautobots/nsavp_tools)
8. <https://www.openstreetmap.org>

## References

- Agarwal S, Vora A, Pandey G, Williams W, Kourous H and McBride J (2020) Ford multi-AV seasonal dataset. *The International Journal of Robotics Research* 39(12): 1367–1376.
- Alonso I and Murillo AC (2019) EV-SegNet: Semantic segmentation for event-based cameras. In: *2019 IEEE/CVF Conference on Computer Vision and Pattern Recognition Workshops (CVPRW)*. Long Beach, CA, USA: IEEE, pp. 1624–1633.
- Arandjelovic R, Gronat P, Torii A, Pajdla T and Sivic J (2016) NetVLAD: CNN architecture for weakly supervised place recognition. In: *2016 IEEE Conference on Computer Vision and Pattern Recognition (CVPR)*. Las Vegas, NV, USA: IEEE, pp. 5297–5307.
- Binas J, Neil D, Liu SC and Delbruck T (2017) DDD17: End-to-end DAVIS driving dataset. *arXiv preprint arXiv:1711.01458*.
- Chaney K, Cladera F, Wang Z, Bisulco A, Hsieh MA, Korpela C, Kumar V, Taylor CJ and Daniilidis K (2023) M3ED: Multi-robot, multi-sensor, multi-environment event dataset. In: *2023 IEEE/CVF Conference on Computer Vision and Pattern Recognition Workshops (CVPRW)*. Vancouver, BC, Canada: IEEE, pp. 4016–4023.
- Chen P, Guan W, Huang F, Zhong Y, Wen W, Hsu LT and Lu P (2023) ECMD: An event-centric multisensory driving dataset for SLAM. *IEEE Transactions on Intelligent Vehicles* : 1–10.
- Cheng W, Luo H, Yang W, Yu L, Chen S and Li W (2019) DET: A high-resolution DVS dataset for lane extraction. In: *2019 IEEE/CVF Conference on Computer Vision and Pattern Recognition Workshops (CVPRW)*. Long Beach, CA, USA: IEEE, pp. 1666–1675.
- Choi Y, Kim N, Hwang S, Park K, Yoon JS, An K and Kweon IS (2018) KAIST multi-spectral day/night data set for autonomous and assisted driving. *IEEE Transactions on Intelligent Transportation Systems* 19(3): 934–948.
- De Tournemire P, Nitti D, Perot E, Migliore D and Sironi A (2020) A large scale event-based detection dataset for automotive. *arXiv preprint arXiv:2001.08499*.
- ElSheikh A, Abu-Nabah BA, Hamdan MO and Tian GY (2023) Infrared camera geometric calibration: A review and a precise thermal radiation checkerboard target. *Sensors* 23(7): 3479.
- Farooq MA, Shariff W and Corcoran P (2023) Evaluation of thermal imaging on embedded GPU platforms for application in vehicular assistance systems. *IEEE Transactions on Intelligent Vehicles* 8(2): 1130–1144.
- Fischer T and Milford M (2020) Event-based visual place recognition with ensembles of temporal windows. *IEEE Robotics and Automation Letters* 5(4): 6924–6931.
- Franchi G, Hariat M, Yu X, Belkhir N, Manzanera A and Filliat D (2024) InfraParis: A multi-modal and multi-task autonomous driving dataset. In: *Proceedings of the IEEE/CVF Winter Conference on Applications of Computer Vision (WACV)*. Waikoloa, HI, USA: IEEE, pp. 2973–2983.
- Furgale P, Rehder J and Siegwart R (2013) Unified temporal and spatial calibration for multi-sensor systems. In: *2013 IEEE/RSJ International Conference on Intelligent Robots and Systems*. Tokyo, Japan: IEEE, pp. 1280–1286.
- Gallego G, Delbruck T, Orchard G, Bartolozzi C, Tabbara B, Censi A, Leutenegger S, Davison AJ, Conradt J, Daniilidis K and Scaramuzza D (2022) Event-based vision: A survey. *IEEE Transactions on Pattern Analysis and Machine Intelligence* 44(1): 154–180.
- Garg S, Suenderhauf N and Milford M (2018) LoST? Appearance-invariant place recognition for opposite viewpoints using visual semantics. In: *Proceedings of Robotics: Science and Systems*. Pittsburgh, Pennsylvania: Robotics: Science and Systems Foundation.
- Gehrig M, Aarents W, Gehrig D and Scaramuzza D (2021) DSEC: A stereo event camera dataset for driving scenarios. *IEEE Robotics and Automation Letters* 6(3): 4947–4954.
- Geiger A, Lenz P, Stiller C and Urtasun R (2013) Vision meets robotics: The KITTI dataset. *The International Journal of Robotics Research* 32(11): 1231–1237.
- Ha Q, Watanabe K, Karasawa T, Ushiku Y and Harada T (2017) MFNet: Towards real-time semantic segmentation for autonomous vehicles with multi-spectral scenes. In: *2017 IEEE/RSJ International Conference on Intelligent Robots and Systems (IROS)*. Vancouver, BC, Canada: IEEE, pp. 5108–5115.
- Hadviger A, Cvišić I, Marković I, Vražić S and Petrović I (2021) Feature-based event stereo visual odometry. In: *2021 European Conference on Mobile Robots (ECMR)*. Bonn, Germany: IEEE, pp. 1–6.

- Hadviger A, Štironja VJ, Cvišić I, Marković I, Vražić S and Petrović I (2023) Stereo visual localization dataset featuring event cameras. In: *2023 European Conference on Mobile Robots (ECMR)*. Coimbra, Portugal: IEEE, pp. 1–6.
- Hu Y, Binas J, Neil D, Liu SC and Delbruck T (2020) DDD20 end-to-end event camera driving dataset: Fusing frames and events with deep learning for improved steering prediction. In: *2020 IEEE 23rd International Conference on Intelligent Transportation Systems (ITSC)*. Rhodes, Greece: IEEE, pp. 1–6.
- Hu Y, Liu SC and Delbruck T (2021) v2e: From video frames to realistic DVS events. In: *2021 IEEE/CVF Conference on Computer Vision and Pattern Recognition Workshops (CVPRW)*. Nashville, TN, USA: IEEE, pp. 1312–1321.
- Huai J, Zhuang Y, Shao Y, Jozkow G, Wang B, Liu J, He Y and Yilmaz A (2023) A review and comparative study of close-range geometric camera calibration tools. *arXiv preprint arXiv:2306.09014*.
- Hutton J, Ip A, Bourke T, Scherzinger B, Gopaul N, Canter P, Oveland I and Blankenberg L (2008) Tight integration of GNSS post-processed virtual reference station with inertial data for increased accuracy and productivity of airborne mapping. *Remote Sensing and Spatial Information Sciences* 37(B5): 829–834.
- Hwang S, Park J, Kim N, Choi Y and Kweon IS (2015) Multispectral pedestrian detection: Benchmark dataset and baseline. In: *2015 IEEE Conference on Computer Vision and Pattern Recognition (CVPR)*. Boston, MA, USA: IEEE, pp. 1037–1045.
- Judd KM, Thornton MP and Richards AA (2019) Automotive sensing: assessing the impact of fog on LWIR, MWIR, SWIR, visible, and lidar performance. In: *Infrared Technology and Applications XLV*. Baltimore, MD, USA: SPIE, pp. 322–334.
- Lee AJ, Cho Y, Shin Ys, Kim A and Myung H (2022) ViViD++ : Vision for visibility dataset. *IEEE Robotics and Automation Letters* 7(3): 6282–6289.
- Ligocki A, Jelinek A and Zalud L (2020) Brno urban dataset - the new data for self-driving agents and mapping tasks. In: *2020 IEEE International Conference on Robotics and Automation (ICRA)*. Paris, France: IEEE, pp. 3284–3290.
- Matthies L and Shafer S (1987) Error modeling in stereo navigation. *IEEE Journal on Robotics and Automation* 3(3): 239–248.
- Milford MJ and Wyeth GF (2012) SeqSLAM: Visual route-based navigation for sunny summer days and stormy winter nights. In: *2012 IEEE International Conference on Robotics and Automation*. Saint Paul, MN, USA: IEEE, pp. 1643–1649.
- Miron A, Rogozan A, Ainouz S, Benschrair A and Broggi A (2015) An evaluation of the pedestrian classification in a multi-domain multi-modality setup. *Sensors* 15(6): 13851–13873.
- Mollica G, Felicioni S, Legittimo M, Meli L, Costante G and Valigi P (2023) MA-VIED: A multisensor automotive visual inertial event dataset. *IEEE Transactions on Intelligent Transportation Systems* : 1–11.
- Muglikar M, Gehrig M, Gehrig D and Scaramuzza D (2021) How to calibrate your event camera. In: *2021 IEEE/CVF Conference on Computer Vision and Pattern Recognition Workshops (CVPRW)*. Nashville, TN, USA: IEEE, pp. 1403–1409.
- Olson E (2011) AprilTag: A robust and flexible visual fiducial system. In: *2011 IEEE International Conference on Robotics and Automation*. Shanghai, China: IEEE, pp. 3400–3407.
- Perot E, de Tournemire P, Nitti D, Masci J and Sironi A (2020) Learning to detect objects with a 1 megapixel event camera. In: *Advances in Neural Information Processing Systems*, volume 33. Curran Associates, Inc., pp. 16639–16652.
- Rebecq H, Ranftl R, Koltun V and Scaramuzza D (2021) High speed and high dynamic range video with an event camera. *IEEE Transactions on Pattern Analysis and Machine Intelligence* 43(6): 1964–1980.
- Scheerlinck C, Rebecq H, Stoffregen T, Barnes N, Mahony R and Scaramuzza D (2019) CED: Color event camera dataset. In: *2019 IEEE/CVF Conference on Computer Vision and Pattern Recognition Workshops (CVPRW)*. Long Beach, CA, USA: IEEE, pp. 1684–1693.
- Shin U, Park J and Kweon IS (2023) Deep depth estimation from thermal image. In: *2023 IEEE/CVF Conference on Computer Vision and Pattern Recognition (CVPR)*. Vancouver, BC, Canada: IEEE, pp. 1043–1053.
- Sironi A, Brambilla M, Bourdis N, Lagorce X and Benosman R (2018) HATS: Histograms of averaged time surfaces for robust event-based object classification. In: *2018 IEEE/CVF Conference on Computer Vision and Pattern Recognition*. Salt Lake City, UT, USA: IEEE, pp. 1731–1740.
- St-Laurent L, Mikhnevich M, Bubel A and Prévost D (2017) Passive calibration board for alignment of VIS-NIR, SWIR and LWIR images. *Quantitative InfraRed Thermography Journal* 14(2): 193–205.
- Sun Z, Messikommer N, Gehrig D and Scaramuzza D (2022) ESS: Learning event-based semantic segmentation from still images. In: *European Conference on Computer Vision*. Tel Aviv, Israel: Springer, pp. 341–357.
- Takumi K, Watanabe K, Ha Q, Tejero-De-Pablos A, Ushiku Y and Harada T (2017) Multispectral object detection for autonomous vehicles. In: *Proceedings of the on Thematic Workshops of ACM Multimedia*. Mountain View, CA, USA: ACM, pp. 35–43.
- Teledyne FLIR (2018) Teledyne FLIR thermal dataset for algorithm training. Available at: <https://www.flir.com/oem/adas/adas-dataset-form/> (accessed 5 December 2023).
- Torres SN and Hayat MM (2003) Kalman filtering for adaptive nonuniformity correction in infrared focal-plane arrays. *Journal of the Optical Society of America A* 20(3): 470–480.
- Tumas P, Nowosielski A and Serackis A (2020) Pedestrian detection in severe weather conditions. *IEEE Access* 8: 62775–62784.
- Ursine W, Calado F, Teixeira G, Diniz H, Silvino S and De Andrade R (2012) Thermal/visible autonomous stereo visio system calibration methodology for non-controlled environments. In: *11th International Conference on Quantitative Infrared Thermography*. Naples, Italy, pp. 1–10.
- Valverde FR, Hurtado JV and Valada A (2021) There is more than meets the eye: Self-supervised multi-object detection and tracking with sound by distilling multimodal knowledge. In: *2021 IEEE/CVF Conference on Computer Vision and Pattern Recognition (CVPR)*. Nashville, TN, USA: IEEE, pp. 11612–11621.
- Vertens J, Zürn J and Burgard W (2020) HeatNet: Bridging the day-night domain gap in semantic segmentation with thermal images. In: *2020 IEEE/RSJ International Conference on Intelligent Robots and Systems (IROS)*. Las Vegas, NV, USA:

- IEEE, pp. 8461–8468.
- Xu Z, Zhuang J, Liu Q, Zhou J and Peng S (2019) Benchmarking a large-scale FIR dataset for on-road pedestrian detection. *Infrared Physics & Technology* 96: 199–208.
- Yun S, Jung M, Kim J, Jung S, Cho Y, Jeon MH, Kim G and Kim A (2022) STheReO: Stereo thermal dataset for research in odometry and mapping. In: *2022 IEEE/RSJ International Conference on Intelligent Robots and Systems (IROS)*. Kyoto, Japan: IEEE, pp. 3857–3864.
- Zhang J, Zhuge H, Liu Y, Peng G, Wu Z, Zhang H, Lyu Q, Li H, Zhao C, Kircali D, Mharolkar S, Yang X, Yi S, Wang Y and Wang D (2023a) NTU4DRadLM: 4D radar-centric multi-modal dataset for localization and mapping. *arXiv preprint arXiv:2309.00962*.
- Zhang Y, Carballo A, Yang H and Takeda K (2023b) Perception and sensing for autonomous vehicles under adverse weather conditions: A survey. *ISPRS Journal of Photogrammetry and Remote Sensing* 196: 146–177.
- Zhu AZ, Thakur D, Özaslan T, Pfrommer B, Kumar V and Daniilidis K (2018) The multivehicle stereo event camera dataset: An event camera dataset for 3D perception. *IEEE Robotics and Automation Letters* 3(3): 2032–2039.